Investigations on the wave performance of Savonius turbine operating under initial phase-locked strategy

Li, Fengschen; Yao, Jianjun; Eskilsson, Claes; Pan, Youcheng; Chen, Junhua; Ji, Renwei

Published in:
Physics of Fluids

DOI (link to publication from Publisher):
10.1063/5.0162835

Publication date:
2023

Document Version
Accepted author manuscript, peer reviewed version

Citation for published version (APA):
Li, F., Yao, J., Eskilsson, C., Pan, Y., Chen, J., & Ji, R. (2023). Investigations on the wave performance of Savonius turbine operating under initial phase-locked strategy. *Physics of Fluids*, *35*(9), Article 097138. https://doi.org/10.1063/5.0162835

Accepted to Phys. Fluids 10.1063/5.0162835

Investigations on the wave performance of Savonius turbine operating under initial phase-locked strategy

Fengshen Li[a,b,c]（李凤甡）, Jianjun Yao[a,*] （姚建均）, Claes Eskilsson[c], Youcheng Pan[d]（潘宥承）, Junhua Chen[e]（陈俊华）, and Renwei Ji[f]（纪仁玮）

[a] College of Mechanical and Electrical Engineering, Harbin Engineering University, Harbin 150001, China;
[b] School of Mechatronics and Energy Engineering, Ningbo Tech University, 315100, Ningbo, China;
[c] Department of the Built Environment, Aalborg University, Thomas Mann Vej 23, DK-9220 Aalborg, Denmark;
[d] School of Architecture, Harbin Institute of Technology, Harbin 150006, China;
[e] College of Science & Technology, Ningbo University, Cixi 315300, China;
[f] College of Shipbuilding Engineering, Harbin Engineering University, Harbin 150001, China;
* Correspondence: Jianjun Yao (travisyao1@126.com); College of Mechanical and Electrical Engineering, Harbin Engineering University; No.145, Nantong Street, Harbin City, Heilongjiang Province 150001, China.

Abstract: Savonius hydrokinetic turbines (SHTs), categorized as emerging cyclic-type wave energy converters (WECs), have demonstrated notable potential in achieving elevated energy conversion efficiency and consistent power output. This performance is particularly observed when operating under the initial phase-locked strategy (IPLS), marking a significant advancement in the realm of wave energy harvesting. However, a thorough exploration of the influences stemming from wave conditions and turbine design remains an area that warrants further investigation for advancing the performance of SHT-WECs under the proper operational strategy. This study undertakes an exhaustive analysis of geometric parameters, encompassing turbine diameter, blade number, and thickness. An experiment-validated numerical model based on the unsteady two-phase Reynolds-averaged Navier-Stokes equations is adopted in the research. Comprehensive investigations include analyses of flow fields around the turbine, pressure distributions on blade surfaces, and dynamic torque variations. These analyses serve to elucidate the variation rules of hydrodynamic characteristics and their influential mechanisms. The results highlight the notable impact of the proposed "relative-short wavelength impact" on the performance of SHT-WECs operating under IPLS conditions. Notably, no significant impact is observed when the relative wavelength exceeds 17. Optimal performance is achieved with the thinnest and two-bladed turbine configuration. Moreover, optimizing the turbine diameter significantly enhances SHT-WEC conversion efficiency, with the attained maximum value reaching approximately 18.6%. This study offers a concise guideline for designing turbine diameters in alignment with specific wave conditions.

Keywords: Savonius hydrokinetic turbine, Wave energy converter, Initial phase-locked strategy, Parametric study, Turbine diameter

1. Introduction

A consistent and dependable energy supply stands as a fundamental requisite for human sustenance and societal progress. The evolution of industrial technologies and the expansion of populations have driven a substantial surge in worldwide energy consumption. The figures have escalated significantly, surging from 13,152 TWh in 2008 to 23,031 TWh in 2018. Projections indicate a further ascent of 58% by 2040, underscoring the pressing need to address the escalating global energy demands.[1]. Extensive extraction of conventional fossil fuels has given rise to many concerns, notably encompassing global warming and atmospheric pollution. Escalating renewable energy generation assumes paramount significance in catering to worldwide power requisites while preserving the integrity of the natural environment. Over the preceding decade, the cumulative installed capacity for renewable energy has surged to approximately 2,500 GW. However, the complete substitution of fossil fuels with renewable energy sources continues to pose a formidable and intricate challenge[2]. The oceans harbor an immense reservoir of renewable energy encompassing diverse manifestations, including wave energy, tidal energy, temperature gradients, and salinity differentials. Notably, the global wave energy potential is approximately 9,000 TWh. This inherent oceanic energy wealth stands poised to play a pivotal role in shaping the future of sustainable energy generation. [3]. Wave energy has the characteristics of clean power generation and is widely distributed [4]. In comparison to other renewable sources like wind and solar, wave energy offers distinct advantages, including enhanced forecastability and substantially higher energy density. However, it does face a primary drawback, characterized by inherent random variability spanning multiple temporal scales. This stochastic nature underscores the challenge of harnessing wave energy consistently and efficiently [5]. With the diverse methods employed for wave energy extraction, coupled with considerations of water depth and device placement, a multitude of wave energy converters have been developed and implemented to facilitate the conversion of wave energy into electrical power generation. This dynamic landscape of innovation and deployment underscores the evolving endeavors aimed at maximizing the utilization of this abundant renewable resource[6]. According to working principles, the wave energy systems are mainly classified as oscillating water columns (OWC, such as LIMPET, Mutriku wave power plant, etc. [7, 8]), oscillating bodies (such as Wavebob, Wave Star, etc. [9-11]), and overtopping devices (such as Wave Dragon, etc. [12]). The apparent drawbacks of wave energy are the high costs of constructing, deploying, and maintaining WECs [6]. Nevertheless, the Savonius hydrokinetic turbine (SHT) presents a straightforward approach to wave energy extraction due to its cost-effective fabrication involving semicircular blades and the direct conversion of wave kinetic energy. This direct energy conversion pathway holds the potential for substantial enhancement in economic viability, indicating a plausible avenue for improved overall economic performance.

Nomenclature

a	Half blade length (m)
a_w	wave amplitude (m)
b	blade width (m)
d	water depth (m)
d_0	overlap distance (m)
D	turbine diameter (m)
D/H	relative turbine diameter (-)
e	overlap ratio (-)
f_r	relative rotation frequency (f_t/f_w)
f_t	turbine rotation frequency (-)
f_w	wave frequency (-)
H	wave height (m)
H/λ	wave steepness (-)
N	blade number
P_{turbine}	power produced by turbine (W)
P_{wave}	theoretical available wave power (W)
Q	turbine torque (N·m)
t	time (s)
t/T	period number
T	wave period (s)
u	flow velocity magnitude (m/s)
u_x	flow velocity in x-direction (m/s)
u_z	flow velocity in z-direction (m/s)

Greek Symbols

α	phase angle (degree)
β	initial phase angle (degree)
θ	blade angle (degree)
λ	wavelength (m)
λ/D	relative wavelength (-)
η_{eff}	energy conversion efficiency (%)
ω	rotational speed (rad/s)
δ	blade thickness (mm)
ε	blade curvature (b/a)

Abbreviation

CFD	computational fluid dynamics
TSR	tip speed ratio
ECE	energy conversion efficiency
NWT	numerical wave tank
PLS	phase-locked strategy
PUS	phase-unlocked strategy
IPLS	initial phase-locked strategy
SHT	Savonius hydrokinetic turbine
SWL	still water level
WEC	wave energy converter

W	turbine width (m)	VOF	volume of fluid
y^+	dimensionless wall distance (-)	RSWI	relative-short wavelength impact
Z	shaft distance to the free surface (m)	OWC	oscillating water column

Although SHT is a new concept of cyclical type WEC when applied to harvesting wave energy, the Savonius turbine (drag-type) has been recognized as an essential branch of turbines for extracting wind and water stream energy since its invention in 1931 [13]. The SHT is particularly advantageous due to its self-startup capability, lower installation and maintenance costs [14], and less emitted noise. However, the SHT suffers from a low efficiency rate, a consequence attributed to its inherently lower operating tip speed ratio (*TSR*) in contrast to lift-type turbines. This disparity arises due to the substantial drag force exerted on the convex surface, resulting in a trade-off between the turbine design and its efficiency performance[15]. Therefore, continuous efforts have been made to enhance the Savonius turbine performance in recent years. For example, placing a deflector redirecting the flow away from the returning blade [16-18], reasonable array arrangement[19-21], and the hybrid lift-type turbine increasing the efficiency [22], etc. are all possible approaches to improve efficiency. However, adjusting the geometric parameters is one of the most effective and primary methods to accomplish the improvement [23]. Numerous studies have focused on optimizing geometric parameters for Savonius turbines applied to capture wind and water stream energy. Talukdar[14] carried out a parametric analysis of the SHT. The performance of the turbine was improved by optimizing the blade profile to a semicircular shape and using two blades. Chan[24] used an evolutionary-based genetic algorithm and computational fluid dynamics (CFD) simulations to optimize the blade shape. Fatahian[25] introduced an innovative solution that involves the dynamic venting of these returning blades through controllable flaps while preserving their omnidirectional capability. Yao[26] explored the effect of parameters concerning different flow velocities. Roy [27] proposed an inverse method for optimizing the geometric parameters of the wind turbine, which effectively reduced the dimensions of the turbine and so on.

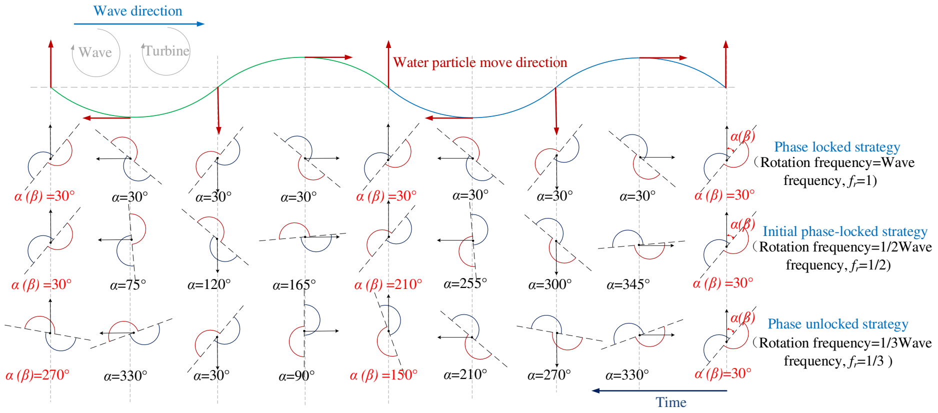

Fig. 1 Operation schematic of different strategies[28].

In contrast, there is a noticeable scarcity of research focused on the geometric parameters of SHT-WECs. Prasad [29] conducted an investigation into the impact of blade entry angles within a numerical wave tank, revealing that the turbine exhibited optimal performance with a blade entry angle of 20°. The blade curvature was optimized to 70° by Ahmed [30] through experimental tests using particle image velocimetry (PIV). Also, Tutar [31] executed an experimental examination within a wave flume, explicitly investigating the optimal blade numbers. The findings highlighted that augmenting the blade count resulted in a notable enhancement of the productive torque output. Besides, two blade shapes with angles of 40° and 60° of Savonius turbine as the components of an OWC system were numerically compared in Zullah's study. [32]

The literature reviewed underscores the efforts of numerous researchers in enhancing the performance of SHT-WECs through geometric parameter optimization. However, it is noteworthy that the prior studies did not account for the operational strategy. Building upon the theoretical dynamic phase angle variation pattern, Li and Yao have introduced three distinct operational strategies [28]. As shown in Fig. 1, they are the phase-locked strategy (PLS), the initial phase-locked strategy (IPLS), and the phase-unlocked strategy (PUS). Under the PLS, the SHT-WEC maintains a constant dynamic phase angle. The IPLS involves the turbine entering each new wave cycle with a consistent phase angle. In the case of the PUS, the dynamic phase angle is allowed to vary freely. Adapting the rotation frequency to establish precise correlations with the regular wave frequency is a prerequisite for operation under distinct strategies. The performance of the SHT-WEC under these three strategies was meticulously analyzed and compared in the previous study[28]. The obtained results of average energy conversion efficiency(ECE) shown in Fig. 2 indicate that the turbine operating under IPLS presents the best performance due to the highest energy conversion efficiency (123% and 58% higher than PLS and PUS T=1.3s). Moreover, from the dynamic torque curves plotted in Fig. 3, it is found that the dynamic torque of IPLS is always positive, largest, and in phase with the wave elevation. Consequently, the so-called IPLS was found to be the optimum operating strategy.

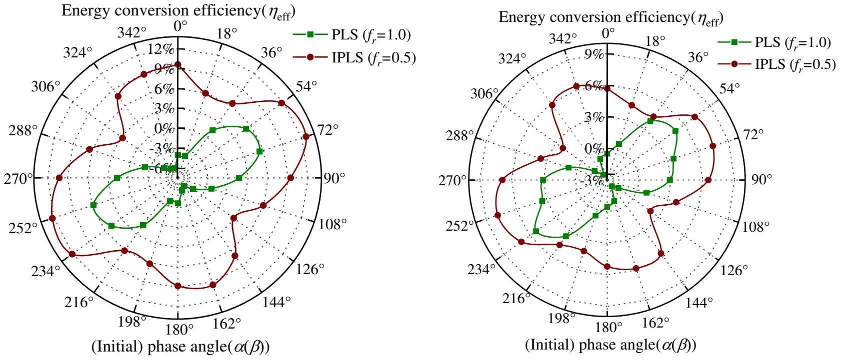

(a) T=1.3s, H=0.18 m

(b) T=1.6s, H=0.18 m

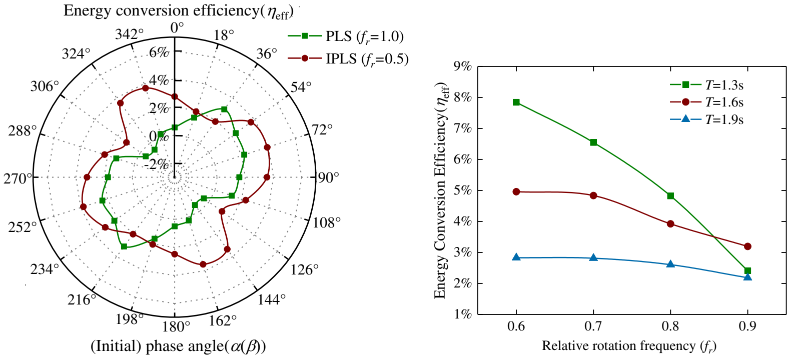

(c) T=1.9s, H=0.18m

(d) SHT operating under PUS.

Fig. 2 The comparison of the average ECE of SHT-WEC operating under three different strategies[28].

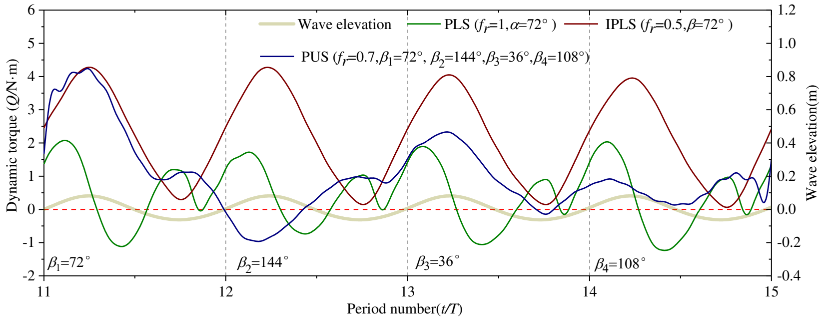

Fig. 3 Time history of the dynamic torque of SHT-WEC operating under three different strategies in four-wave cycle time (T=1.3s, H=0.18m)[28].

This study will extend its investigation to delve into the influence of wave parameters and fundamental geometric variables, encompassing turbine diameter, blade number, and thickness, on the performance of the SHT-WEC operating under the optimal strategy (IPLS). The major limitation of IPLS is the fixed relationship between the rotation speed and the wave period. Particularly in the case of the two-bladed turbine, this ratio is established at half of the wave period. Nevertheless, as the blade number increases to three and four, the SHT profile alteration periods decrease to 120° and 90°, respectively. Consequently, multi-bladed SHT-WECs offer an expanded spectrum of potential relative rotation frequencies during IPLS operation. Moreover, the preceding investigation failed to identify the emergence of high-velocity vortices encompassing the blade tip perimeters; instead, water particles collided with these regions, resulting in a substantial generation of torque [28]. The magnitude of the blade's thickness influences the configuration of the tip edge. Consequently, it is both logically and substantively justified to delve into the prospect of enhancing the SHT-WEC's capacity by auguring blade number and thickness.

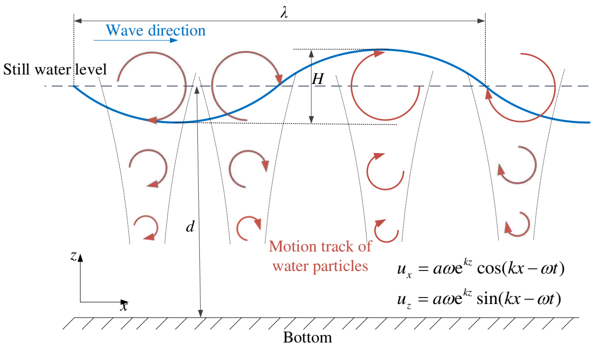

Fig. 4. Wave-induced water particle motion in deep water.

The exploration of turbine diameter has been relatively sparse in the conventional context of SHT applications for harnessing stream energy, such as wind and tide. While the turbine size directly correlates with power output and the theoretical incoming stream energy, its diameter remains inconsequential when calculating the pivotal power coefficient. However, the examination of turbine diameter assumes significance when considering SHT-WEC operation under IPLS, driven by three key rationales. Firstly, the diameter exerts a palpable influence on energy conversion efficiency, owing to its proportional linkage with power output, albeit lacking correlation with the theoretically available wave power. Secondly, the non-uniform distribution of velocity vectors along the horizontal plane of wave propagation impacts turbine performance, particularly when the turbine diameter assumes a relatively substantial dimension. Lastly, the diameter emerges as the pivotal variable dictating the operational parameter of the tip speed ratio (*TSR*) due to the relatively fixed rotation speed.

The illustration of water particle motion induced by wave dynamics is presented in Fig. 4. In contrast to the uniform incoming flow found in streams, the direction and velocity of water particles within a wave exhibit cyclic variations. As depicted by the discrete relationships illustrated for deep waves in Fig. 4, the velocity is primarily influenced by wave amplitude, frequency, and the distance of water particles from the still water level (SWL). For instance, in the case of a two-bladed turbine operating under IPLS, the rotational frequency is consistently set at half the wave frequency. Consequently, the turbine's diameter governs both the tip speed and the spatial proximity of water particles around the blade's edge to the SWL, thereby impacting the tip speed ratio (*TSR*). In this context, the strategic design of the turbine's diameter assumes significance as an effective means of adjusting the *TSR* to a favorable range, thereby enhancing overall performance.

Given the above fact, the present work aims to enhance the performance of SHT-WEC operating under the initial phase-locked strategy. It can be expected that optimizing the turbine design according to the wave condition may significantly improve the performance of the SHT-WEC operating under IPLS. The methodology is to perform a parametric study using a validated numerical wave tank. Following the introduction in Section 1, the SHT-WEC and related parameters are presented in section 2. Section 3 outlines the numerical model adopted in this research; then, the numerical model is validated against physical tests in section 4. In section 5, the performance of SHT-WEC operating under various wave parameters and with different blade numbers, thickness, and turbine diameters, is evaluated in terms of average torque, power output, and energy conversion efficiency. Detailed analysis of the time history of dynamic torque, pressure distributions on the blades, and velocity distributions around the rotating turbines are carried out to reveal the underlying mechanisms and explain the results. Conclusions are presented in section 6.

2. Savonius turbine and parameters definition

Fig. 5 shows the SHT-WEC, and its most critical geometric parameters, including turbine diameter (D), blade number (N), blade thickness (δ), blade curvature (ε), and overlap ratio (e). The overlap ratio is the specific value of overlap distance (d_0) and turbine diameter (D), and the blade curvature is described by the ratio of half-blade length (a) and width (b). Additionally, the 3-dimensional geometric parameters of aspect ratio, which is defined as the ratio of turbine width (W) and diameter (D), end plant, and the helical blade [33], also play an essential role in improving performance. The current investigation adopts a conventional two-bladed Savonius turbine featuring semicircular blades as the foundational turbine geometry, as depicted in Fig. 5. Throughout the entirety of this study, the overlap ratio remains steadfastly set at its optimal value of 0.15 to effectively mitigate the generation of adverse negative torque on the returning blade[34]. Other parameter configurations explored in this study are listed in Table 1.

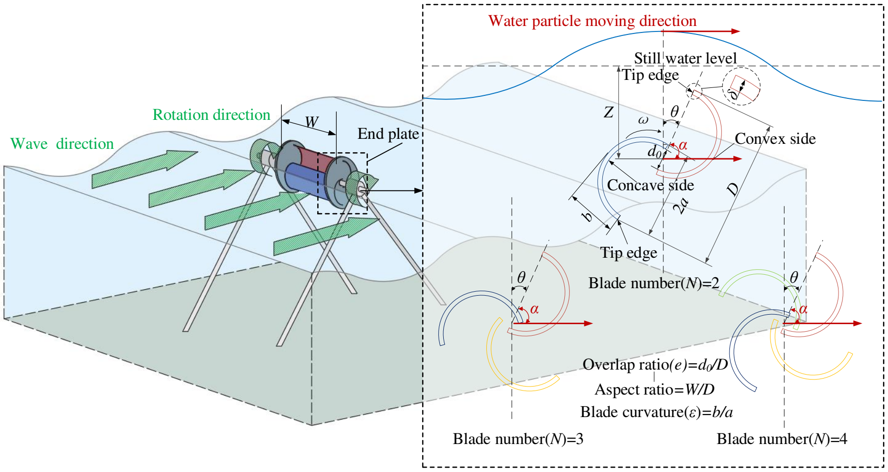

Fig. 5. Schematic of the Savonius hydrokinetic turbine (SHT).

In the conventional utilization of SHT for harnessing tidal energy, the governing operational parameters encompass the tip speed ratio (*TSR*) and the blade angle (θ). Nevertheless, when delving into the performance analysis of SHT-WEC, an additional set of four pivotal parameters comes under scrutiny: phase angle (α), initial phase angle (β), relative rotation frequency (f_r), and submersion level (Z). The phase angle is the key parameter in classifying the operating strategy. It is defined as the angle from the theoretical water particle direction to the turbine axis, as shown in Fig. 5. The initial phase angle is the phase angle of the turbine entering every new wave cycle, as shown in Fig. 1. In the case of SHT-WECs operating under IPLS, the relative rotation frequency is maintained as a constant fraction: 1/2 for a two-bladed turbine, 1/3 and 2/3 for a three-bladed turbine, and 1/4, 1/2, and 3/4 for a four-bladed turbine.

Furthermore, the effects of different initial phase angles and submersion levels have been discussed in [28]. The initial phase angle of 72° and the submerged level of 0.75 *D* was reported to be optimal, and thus these values are used in the present study. The *TSR* and f_r are defined as:

$$TSR = \frac{\omega D}{2u} \tag{1}$$

$$f_r = \frac{f_w}{f_t} \tag{2}$$

Where f_w and f_t are the wave and turbine rotation frequency, ω is the rotation speed (rad/s), D is the turbine diameter (m), u is the magnitude of flow speed (m/s). The regular wave conditions are defined by wave height (H) and wave period (T), see Table 1. The correspondent wavelength (λ) for a deep-water wave is computed based on the following equation:

$$\lambda = \frac{gT^2}{2\pi} \tag{3}$$

Where g is the gravitational acceleration (9.81 m/s^2). The performance parameters used to evaluate the performance of SHT-WEC are the torque generated by the turbine (Q), the associated power produced by the turbine(P_{turbine})and the energy conversion efficiency (ECE, η_{eff}). They are calculated by:

$$P_{\text{turbine}} = Q\omega \tag{4}$$

$$\eta_{\text{eff}} = \frac{P_{\text{turbine}}}{P_{\text{wave}}} \tag{5}$$

Where ω is the rotation speed (rad/s), and P_{wave} is the theoretical wave power defined by:

$$P_{\text{wave}} = \frac{1}{16}\rho g H^2 \frac{\lambda}{T} W \left[1 + \frac{2kd}{\sinh(2kd)}\right] \tag{6}$$

where ρ is the water density (999 kg/m^3), W is the width of the turbine (m), k is the wave number ($2\pi/\lambda$), and d is the water depth (m). Equation (6) shows that the theoretical wave power is unrelated to the turbine diameter.

Table 1. The related parameters in this study

Parameters	Value
Geometrical parameters:	
Number of blades (N)	2, 3, 4
Turbine diameters (D)	0.36m, 0.405m, 0.45m, 0.495m, 0.54m
Blade thickness (δ)	0.00mm, 1.50mm, 3.00mm, 4.50mm, 6.00mm
Blade curvature (ε)	1.00
Overlap ratio (e)	0.15
Operating parameters	
Submersion level (Z)	0.75D m
Initial phase angle (β)	72°(two-bladed), 0°-342°(three-, four-bladed),
Relative rotation frequency (f_r)	1/2 (two-bladed); 1/3, 2/3 (three-bladed); 1/4, 1/2, 3/4 (four-bladed)
Wave conditions:	
Wave period (T)	0.80s - 2.60s
Wave height (H)	0.06m, 0.08m, 0.1m, 0.18m

3. Numerical model

In this study, the commercial CFD software STAR-CCM+ was utilized to simulate and elucidate the wave-turbine interactions of the SHT-WEC with diverse parameters within the numerical wave tank (NWT). The fundamental governing equations employed for solving the viscous flow comprise mass continuity and momentum conservation, as expressed below:

$$\frac{\partial \rho}{\partial t} + \nabla\cdot\rho \mathrm{U} = 0 \tag{7}$$

$$\frac{\partial}{\partial t}\rho \mathrm{U} + \nabla\cdot\rho \mathrm{U} = -\nabla p + \nabla\cdot\tau \tag{8}$$

Where U is the velocity vector, p is the static pressure and the τ is the shear stress tensor. As the investigated geometric parameters (turbine diameter, blade number and thickness) are all two-dimensional (2D) parameters, 2D simulations are deemed sufficient for this study.

3.1 Simulation model

The numerical wave tank is based on the two-phase Reynolds-Averaged Navier-Stokes (RANS) equations [35]. The standard k-ε turbulent model is used in the present simulation to govern the Reynolds Stress by introducing two new variables, the turbulent kinetic energy (k) and the turbulent dissipation rate (ε), into the RANS equations to describe the unsteady, viscous and incompressible liquid [36]. The momentum equation (8) becomes [37]:

$$\frac{\partial \rho \mathrm{U}}{\partial t} + \nabla\cdot(\rho \mathrm{U}\mathrm{U}) - \nabla\cdot(\mu_{eff}\nabla \mathrm{U}) = -\nabla p' + \nabla\cdot(\mu_{eff}\nabla \mathrm{U})^T + S_M \tag{9}$$

Where S_M is the total body forces, u_{eff} is the effective viscosity equal to:

$$\mu_{eff} = \mu + \mu_t \tag{10}$$

For the k-ε turbulent model, the turbulence viscosity μ_t is defined by:

$$\mu_t = C_\mu \frac{k^2}{\varepsilon} \tag{11}$$

Where C_μ is a constant. The values of k and ε come directly from the following equations:

$$\frac{\partial(\rho k)}{\partial t} + \nabla\cdot(\rho k \mathrm{U}) = \nabla\cdot\left[\left(\mu + \frac{\mu_t}{\sigma_k}\right)\nabla k\right] + P_k - \rho\varepsilon \tag{12}$$

$$\frac{\partial(\rho\varepsilon)}{\partial t} + \nabla\cdot(\rho\varepsilon \mathrm{U}) = \nabla\cdot\left[\left(\mu + \frac{\mu_t}{\sigma_\varepsilon}\right)\nabla\varepsilon\right] + \frac{\varepsilon}{k}(C_{\varepsilon1}P_k - C_{\varepsilon2}\rho\varepsilon) \tag{13}$$

Where σ_k, σ_ε, $C_{\varepsilon1}$ and $C_{\varepsilon2}$ are all constants. P_k is the turbulence production defined by:

$$P_k = \mu_t \nabla \mathrm{U}\cdot(\nabla \mathrm{U} + \nabla \mathrm{U}^T) - \frac{2}{3}\nabla\cdot\mathrm{U}(3\mu_t \nabla \mathrm{U} + \rho_k) + P_{kb} \tag{14}$$

The Volume of Fluid (VOF) multiphase model is utilized to simulate the behavior of two immiscible fluids: liquid and gas. These fluids are treated as a single effective fluid and are computed simultaneously across the entire domain to represent and delineate the free surface. In the VOF function, the α_l is used to describe the fraction of water in a cell, which means, for the full water cell, the VOF function $\alpha_l=1$, for the full air cell, $\alpha_l=0$, and for the cell which is a mixture of the two fluids, $0<\alpha_l<1$.

3.2 Computational domain and boundary conditions

The computational domain and boundary conditions are depicted in Fig. 6. The entire domain consists of three distinct subdomains: (i) the rotating domain, facilitating the turbine's rotation through the overset method; (ii) the stationary domain; and (iii) the wave damping domain introduced to prevent undesired wave reflection. The turbine is placed at the center in the horizontal direction, 5λ from the inlet and outlets of the domain, which is sufficient to avoid the influence of reflected waves and wave damping on the wave profile close to the turbine [29]. The water depth was set to λ, thus, meet the requirement of deep-water waves. Concerning the boundary conditions, the velocity field and the volume fraction are prescribed at the inlet based on the fifth-order Stokes wave theory principles [38]. At the outlet boundary, a pressure outlet boundary condition is employed. Additionally, as illustrated in Fig. 6, a vertical resistance term is incorporated into the vertical velocity equation within a region extending 2λ wide from the outlet boundary. This inclusion serves to dampen the wave effects [39]. The atmosphere boundary was also set to a pressure outlet. Finally, wall boundary and no-slip conditions were imposed on the bottom and all turbine blades.

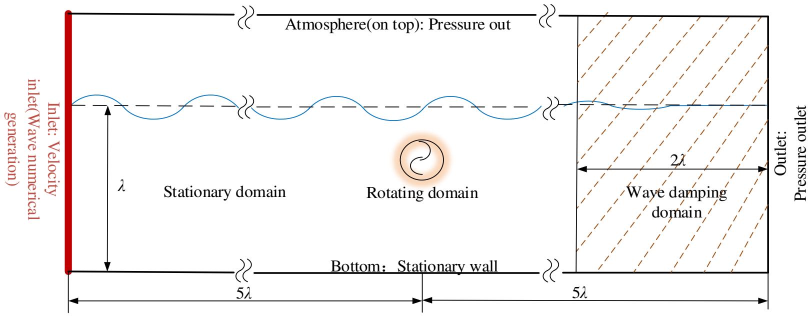

Fig. 6. The computational domain and boundary conditions.

3.3 Grid generation and model set-up

In the computational mesh overview, as depicted in Fig. 7(a), blue represents the water phase within the stationary domain, while yellow indicates the air phase. The rotating domain is represented in brown. Structured grids were utilized in the stationary domain to mitigate truncation errors and computational expenses for simulating wave evolution. However, unstructured polyhedral grids were employed to discretize the rotating domain to represent the circular arc blades accurately. In the free surface zone, the cell size was generally set to the height of 0.05H, and the wave steepness determined the aspect ratio. Body rotation can typically be realized through two methods: (i) the sliding mesh approach and (ii) the overset mesh technique. This study employed the latter method, as illustrated in Fig. 7(b). Additionally, Fig. 7(c) depicts that the overset and stationary background mesh cells within the overset region share comparable sizes, ensuring dependable data transmission and maintaining mass and momentum conservation across the interface.

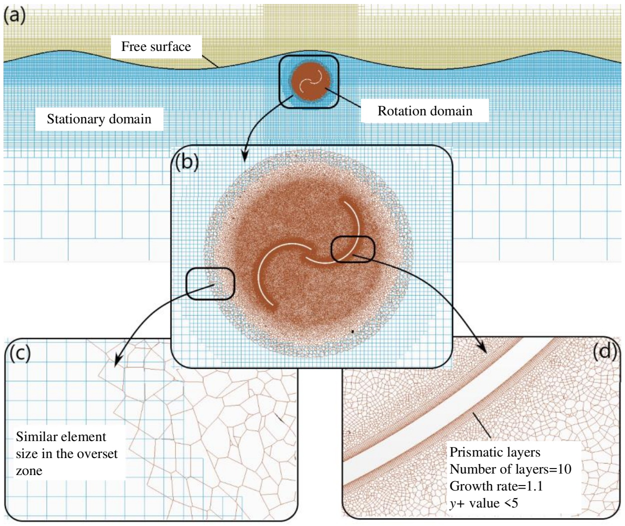

Fig. 7. Computational mesh: (a) The overall mesh; (b) Mesh around the rotating domain; (c) Close-up on the overlap between the background mesh and the overset region; (d) The boundary layer mesh around the blade.

The mesh was refined around the turbine, and ten prismatic layers were generated on the blade surfaces, as shown in Fig. 7(d). The thickness of the first layer mesh was defined appropriately to have a y^+ value less than 5 for reaching the requirement of the all- y^+ wall treatment function and the standard k-ε turbulent model. A second-order time differencing scheme was assumed to prevent attenuation in simulating wave propagation [28]. The time step was set based on the variation of the Courant number in the free surface, which was required to be below five. Additionally, the rotation angle should be less than 1 degree in a one-time step.

Fig. 8 provides a comparison between simulation, theoretical, and experimental results in a condition without the SHT, serving as a validation of wave evolution in the numerical wave tank. The simulated wave evolution closely aligns with theoretical and experimental values, exhibiting only marginal decay around peak and trough points. The maximum attenuation remains under 5%, a deemed acceptable range. To assess grid independence, a study was conducted on the dynamic torque variation produced by the turbine using three different total cell numbers (354,000, 218,000, and 153,000), as depicted in Fig. 9. With an increase in grid count from 218,000 to 354,000, no significant disparity between the two curves emerged. Consequently, a mesh of around 218,000 elements is sufficient to predict the SHT-WEC's performance. It is important to emphasize that the cell number is not constant across all simulations, as mesh configurations vary due to distinct blade numbers, turbine sizes, and wave steepnesses.

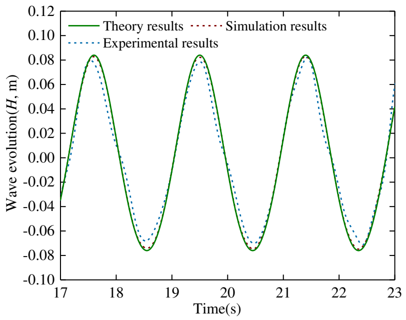

Fig. 8. The wave evolution comparison (*H*=0.16 m, *T*=1.9 s, and *d*=2.5m)

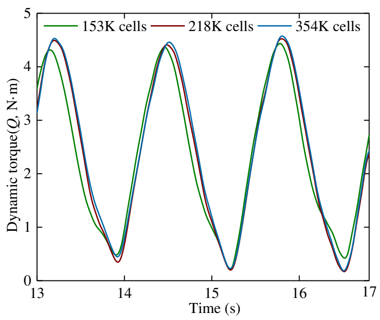

Fig. 9. Grid independence test.

4. Validation of the numerical model

4.1 Experimental set-up

A physical experiment was conducted in a wave flume to validate the numerical simulation model. The working section of the flume spans 70 m in length, 4 m in width and possesses a water depth of 2.5 m. As shown in Fig. 10(a), the flume is equipped with a flap-type wavemaker and a wave-absorbing beach. The maximum regular wave height generated is 0.3 m. From Fig. 10(b), it can be seen that the position of the test section was placed far enough away from the wavemaker to guarantee a fully developed wave profile.

Fig. 10(c) illustrates that the turbine was constructed using a less dense aluminum alloy to diminish the moment of inertia. The physical dimensions of the turbine are outlined in Table 2. Endplates with 0.35 m diameter were installed on both sides of the physical turbine. Two parallel beams supported the turbine shaft through low-friction ball bearings, as shown in Fig. 10(c). The timing belt was applied to drive between the turbine and the transducer. The position of the turbine and the transducer can be adjusted on the truss to ensure the tension of the transmission belt.

In Fig. 11, it can be observed that the dynamic torque transducer (CYT-302) was utilized to capture the dynamic torque produced by the turbine along with its rotational speed. The frequency output signal from CYT-302 was converted into a voltage analog signal (ranging from 0 to 10V) via the F/V conversion module. This signal could then be identified and digitized using the high-speed multifunction USB data acquisition (DAQ) device (USB-1608G). It is important to note that during the experimental tests, the turbine rotated freely in response to the waves. Consequently, the generated torque was too minute to measure by the transducer precisely. Thus, in the present study, only the dynamic rotational speed was utilized to validate the numerical model.

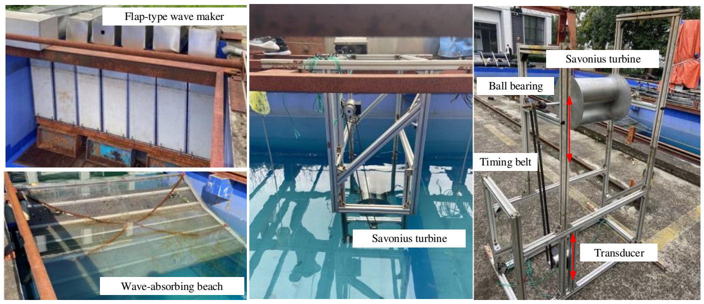

(a) (b) (c)

Fig. 10 Experimental test set-up: (a) the wave-making system; (b) the experimental arrangement; (c) the suspended platform.

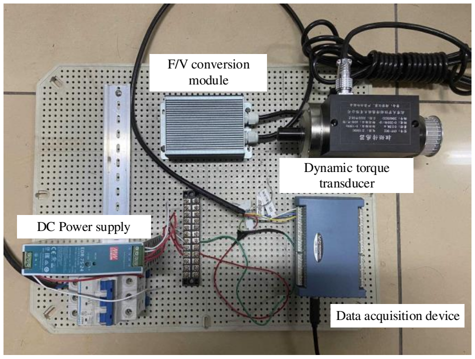

Fig. 11 Experimental measurement system.

Table 2. The experimental SHT-WEC specifications

Specification	**Value**
Number of blades	2
Turbine width (m)	0.40
Outer diameter (m)	0.30
Blade shape	Semicircle
Blade length (m)	0.17
Blade thickness (m)	0.002
Endplate diameter (m)	0.35
Overlap	0.15
Submergence level (m)	0.225(0.75*D*)

4.2 Comparison of experimental and numerical results

Fig.11 presents a comparison between the average rotational speed of the turbine obtained through physical tests and numerical simulations across various wave parameters. The data points displayed in the three graphs (Fig. 12(a)-(c)) exhibit similar overall trends. However, a certain level of deviation is evident between the simulation and experimental outcomes, and this discrepancy follows a distinct pattern with variations in wave height. Compared to the experimental values, the simulations generally over-predicted the rotational speed for the lower wave height. Still, as the wave height increased, the simulation results gradually approached the experimental data, and for larger wave heights, the simulated rotational speeds are under-predicted. Moreover, for the lower wave heights, the over-prediction is more prominent for the longer wave periods.

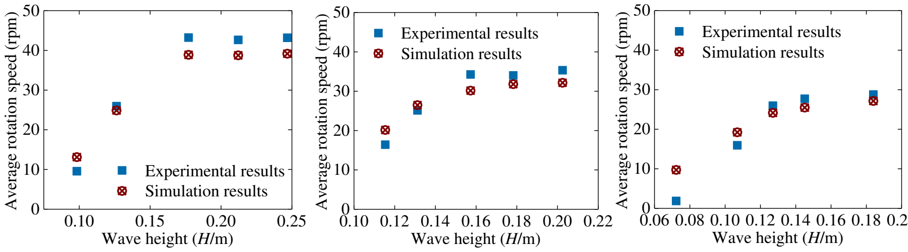

(a) *T*=1.3 s (b) *T*=1.6 s (c)*T*=1.9 s

Fig. 12. Comparison between numerical and experimental rotational speeds versus wave height.

The gradual increase in experimental results can be primarily attributed to the dimensional effect, arising from the disparities between the 3D physical turbine model used in experiments and the 2D numerical turbine model employed in simulations. The limitations of the 2D simulations prevent the capture of potential influences stemming from factors like endplates and aspect ratio. Another contributing factor is the wave profile. The experimental wave generation system is constrained, producing linear waves within the experimental tank. In contrast, the numerical wave tank employs a boundary-driven technique to generate non-linear 5th-order Stokes waves, striving to emulate natural ocean wave conditions closely. Non-linear waveforms inherently exhibit asymmetry between crests and troughs, featuring steeper crests and flatter troughs.

Additionally, low wave heights resulted in greater rotation speeds primarily because of mechanical friction in the physical testing apparatus, impeding the rotation of the turbine. When wave heights are relatively low, the resistance generated by the fluid on the turbine results in minor frictional effects, significantly influencing the rotation speed. However, as wave heights increase, the oscillations of the waves become more intense, leading to a substantial rise in the torque exerted on the turbine. At this point, the impact of frictional forces becomes negligible.

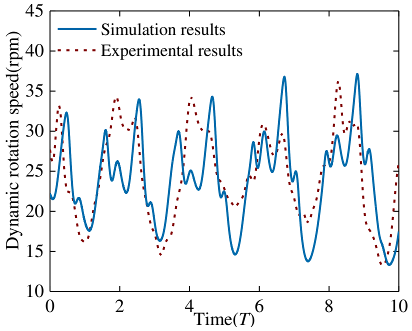

Fig. 13. Comparison between numerical and experimental time domain rotational speeds.

A comparison of the time history rotation speed curves shown in Fig. 13 for the turbine under the wave condition of T=1.9 s, H=0.14 m, indicates that the alignment between the two curves is not optimal. This discrepancy can be attributed to the construction of the water turbine using aluminum alloy material. In its unloaded state, the turbine possesses a relatively low moment of inertia, rendering its dynamic response more susceptible to the impact of uncertain factors such as wave breaking, wave reflection, and turbulence.

In summary, it is evident that while the alignment between the two curves compared in Fig. 13 is not notably high, they exhibit two distinct shared characteristics: firstly, they both demonstrate periodic variations that follow the evolution of the waves; secondly, within each cycle, a multi-peak trend is observable. Moreover, the averaged results in Fig. 12 depict a similar trend, displaying a comparatively minor level of deviation. As such, validation through experimental data confirms that the established two-dimensional simulation model in this section is suitable for predicting the wave energy capture performance of the SHT-WEC.

5. Results and discussion

The validated 2-D simulation model was employed to explore the impact of several factors on the performance of SHT-WEC operating under the IPLS. These factors include (i) wave parameters, (ii) blade number, (iii) blade thickness, and (iv) turbine diameter. The key performance parameters, average torque (Q, N·m), power output (P_{turbine}, W), and energy conversion efficiency (ECE, η_{eff}, %), were computed for analysis.

5.1 Wave parameters

The simulation results of the average torque, power output, and energy conversion efficiency of the turbine operating in IPLS under various wave conditions (H = [0.1, 0.08, 0.06] m and T = [0.8, 1.0, …, 2.4] s) are presented in Fig. 14. The torque generated by the turbine and subsequent power generation exhibits an evident rise with increasing wave height, as illustrated in Fig. 14(a)-(b). This observation aligns with the findings by Tutar [40]. However, Fig. 14(c) reveals that wave height ceases to influence the efficiency of the SHT-WEC once the wave period surpasses 1.8s. Regarding the wave periods, the variation trend of the curves in Fig. 14(a) indicated that torque produced by the turbine rises with increasing wave period, plateauing for periods exceeding T=1.8 s. The power output and ECE curves illustrated in Fig. 14(b)-(c) display an initial upward trend before reaching peak values, followed by a subsequent decline. Moreover, in comparison to power output, the decrease in ECE is more pronounced, with differing wave periods yielding peak values for different wave heights.

From wave kinematics, it is well-known that for a fixed wave period, a larger wave height means a faster motion of the water particles under the wave, which results in the water particles getting more momentum to collide with the blade surface producing torque. The IPLS requires the turbine to rotate at half of the wave frequency, which means the rotation speed is unchanged with the wave height, leading to an increase in power generation due to the higher torque associated with a larger wave height. It is worth noting that the difference in power output for the different wave heights, as identified in Fig. 14 (b) reduces and stabilizes with increasing wave periods. Then, the increments in the power output and theoretical wave energy caused by the higher wave height are equal. As a result, the wave height will have no noticeable effect on the ECE after raising the wave period to 1.8s, as shown in Fig. 14 (c).

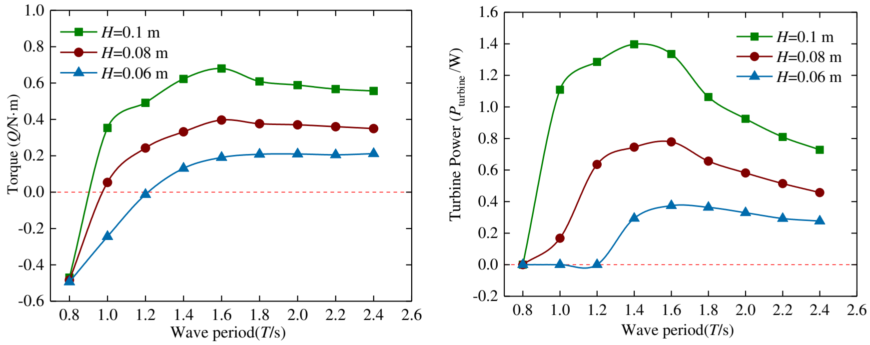

(a) Torque(Q , N·m) (b) Power output($P_{turbine}$,W)

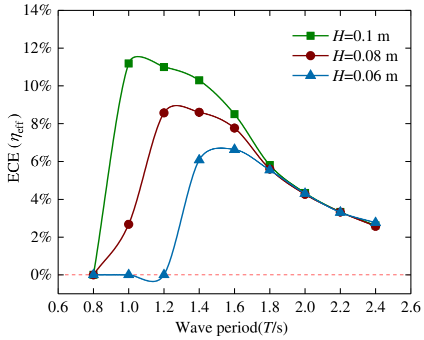

(c) Energy conversion efficiency(η_{eff})

Fig. 14. Average torque, power output, and energy conversion of SHT-WEC operating under IPLS with different wave parameters.

Although the water particles have a higher velocity for a constant wave height in a shorter wave period, the turbine performs worse. The produced torque even becomes negative under several shortest wave periods, which means the SHT-WEC not only can not extract wave energy but also need to obtain extra power from other devices to maintain the rotation. It proves the mentioned hypothesis that short wavelengths would impact performance. This result can be accounted for through the comparison of the flow variation around the turbine operating in different wave periods, as shown in Fig. 15. When the wave period is short (T=0.8 s), as shown in Fig. 15(a), the corresponding wavelength is small enough compared to the turbine diameter, leading to a non-uniform wave-induced velocity distribution over the turbine. This causes the water particles in the upper left area of the turbine, as marked in Fig. 15(a), to move towards and collide with the convex surface of the advancing blade. The result is a low-velocity zone forming around the edge of the convex side generating significantly negative torque on the blade. Although an apparent high-velocity zone can be identified around the convex side, as marked in Fig. 15(a), the area is close to the rotation center, yielding only limited production of positive torque. Moreover, the flow velocity magnitude around the concave surface of the red blade is obviously higher than the convex surface. As shown in Fig. 15(b), when the wave period increases to T=1.2 s, the wavelength becomes longer, and the wave-induced flow field distribution around the turbine becomes more uniform. Comparing the same upper left marked area in Fig. 15(a), the motion direction of the flow particles is almost the same as the turbine rotating direction. As a result, no low-velocity zone can be observed around the advancing blade's convex surface. The high-velocity zone also disappears around the concave surface of the returning blade. The phenomenon of deteriorating turbine performance due to the non-uniform wave-induced velocity field associated with shorter wavelengths is denoted as "relative-short wavelength impact" (RWSI) in this study.

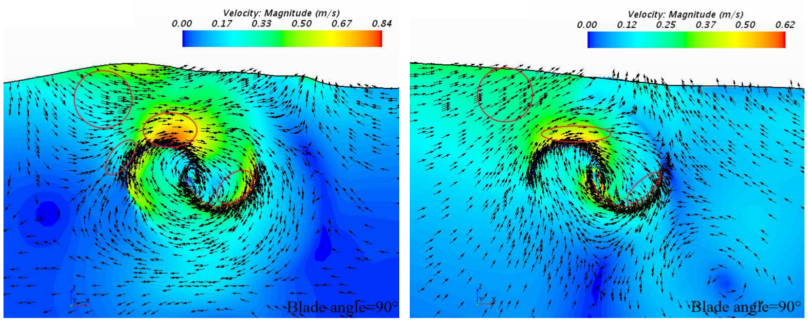

(a) T=0.8 s (b) T=1.2 s

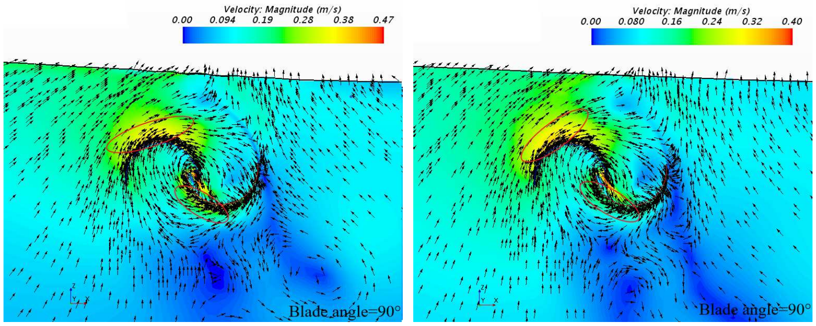

(c) T=1.6 s (d) T=2.0 s

Fig. 15 The velocity vector around the rotating turbine under different wave periods (T=0.8, 1.2, 1.6, 2.0 s; H= 0.08m).

Because the turbine is placed near the SWL and the wave period is long enough, the e^{kz} in equations described in Fig. 4 are close to 1, which means the wave-induced water particles' motion velocity is proportional to the wave frequency. The tip speed of the SHT operating under IPLS is proportional to the wave frequency. As a result, the wave frequency has no effect on the tip speed ratio (*TSR*). Additionally, when the wavelength is long enough, the RSWI will disappear. These two main reasons cause the torque tends to be stable after T=1.8 s. It can be proven by comparing Fig. 15(c) and Fig. 15(d) that these two pictures show no significant difference in the flow fields around turbines. Consequently, the performance of SHT-WECs presents a proportional increase with wave height, as expected. The effect of the wave period on the performance is due to the "relative-short wavelength impact", which will disappear when the wave period further increases after T=1.8 s, or in other words, when the wavelength is longer than 17D ($\lambda/D=17$).

5.2 Blade number

In order to control the turbine with different blade numbers operating under the IPLS, the rotation speed is set as listed in Table 3. For accurately estimating the performance and finding the optimum initial phase angle, 20 initial phase angles (changed from 0° to 342°) are explored in each blade number investigation. The average ECEs of multi-bladed turbines with different initial phase angles (calculated based on the values of five wave periods after the initial start-up transient has diminished) are shown in Fig. 16.

Table 3. The rotation setup of the turbine with different blades operating under IPLS

Blade number (N)	**Relative rotation frequency(f_r)**	**Wave period(T)**	**Rotation speed(ω)**
2	1/2	1.3s	2.416 rad/s
3	1/3		1.611rad/s
	2/3		3.222rad/s
4	1/4		1.208rad/s
	1/2		2.416rad/s
	3/4		3.624rad/s

It was found that the two-bladed SHT-WEC obtained the maximum ECE of around 12.4%[26], operating under IPLS with the initial phase angle of 72° and 252°, as shown in Fig. 2(a). Fig. 16(a) indicates that the maximum ECE for the three-bladed turbine rotating with $f_r = 1/3$ is 6.4% and obtained at $\beta = 0^\circ$, $\beta = 108^\circ$ and $\beta = 234^\circ$. In comparison, the initial phase angle effect is much more significant for the three-bladed turbine rotating with, and the turbine performs better. The highest ECE of almost 12% is found at the different initial phase angles of 18°,126°, and 252°. Although four-bladed turbines have more options of relative rotation frequency that meet the requirement for operating under IPLS, it presents the worst performance. Fig. 16(b) shows that the optimum ECE of around 4.0% ($f_r = 1/4$), 8.0% ($f_r = 1/2$), and 5.1% ($f_r = 3/4$) are found at the initial phase angle of 54°, 144°, 234°, 324°($f_r = 1/4$); 0°, 90°, 180°, 270° ($f_r = 1/2$), and 54°, 144°, 234°, 324°($f_r = 3/4$).

Comparing the obtained results of SHT-WECs with different blade numbers, the ECE decreases with increasing blade numbers. It is worth noting that the multi-bladed SHT-WECs operating under IPLS can adjust the rotation speed to higher values (3.22 rad/s and 3.624 rad/s) than the two-bladed (2.416 rad/s), the multi-bladed turbines do not perform better as might be expected. The average torque shown in Fig. 17 indicates that the torque declines with increasing blade number and relative rotation frequency. In scenarios where the blade number is increased from two to four, and the relative rotation frequency is heightened from 1/2 to 3/4, the maximum torque experiences a substantial reduction of nearly 43% and 52%, respectively, compared to the two-bladed SHT-WEC. However, the incremental rise in rotation speed falls significantly short of compensating for the considerable loss in torque generation. It illustrates that the effect of blade numbers operating under IPLS has a similar trend, as found in the study of Tutar [31].

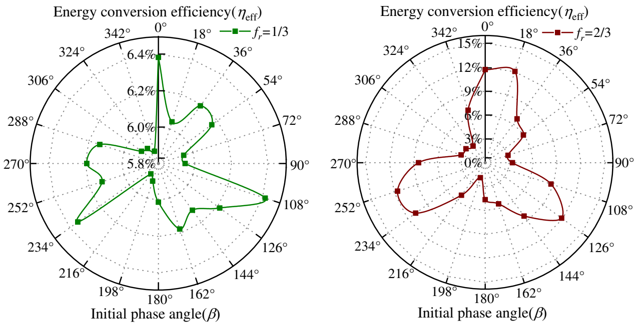

(a) Blade number N=3

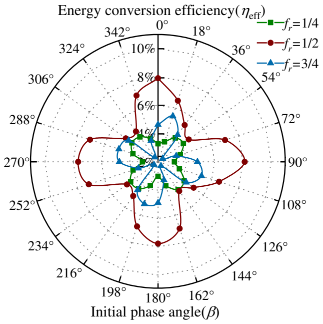

(b) Blade number N=4

Fig. 16. The average energy conversion efficiency (ECE, η_{eff} , %) of SHT operating under IPLS with different turbine blade numbers (T=1.3 s; H= 0.18m).

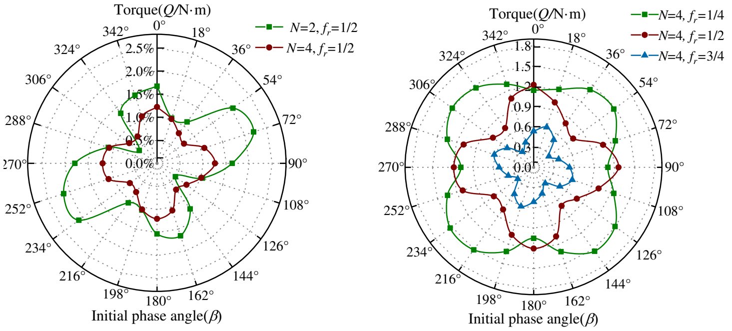

(a) Relative rotation frequency f_r =1/2 (b) Blade number N=4

Fig. 17. The average torque (Q , N·m)) of SHT operating under IPLS with different turbine blade numbers (T=1.3 s; H= 0.18m).

The time history of dynamic torque of two-, three-, and four-bladed SHT-WECs having the highest ECEs are presented in Fig. 18. All three curves vary periodically with the wave elevation. The two-bladed turbine's generated torque is higher overall except for the part around the trough (T+0.75T). The flow field variation around the turbine with different blade numbers in one wave cycle is compared in Fig. 19 to illustrate the influence of the number of blades. Fig. 19(a) and

Fig. 19(b) show that although the blade number increases, the apparent high-velocity zone associated with the low-pressure zone can only be identified around one convex blade surface of the rotating turbine. It means that the added blade can not provide adequate positive torque and even is nearly negative. Thus, the curve around *T*+0.25*T* of generated dynamic torque on the two-bladed turbine plotted in Fig. 18 is much higher. However, with the further evolution of the wave cycle, the performance of the two-bladed turbine reduces sharply. Upon comparing Fig. 19(b) with (c) and (d), it is evident that the previously prominent high-velocity zone diminishes in significance. In fact, its presence around the convex surface of the two-bladed turbine, as depicted in Fig. 19(d), becomes notably inconspicuous, thereby contributing to a reduction in the overall generated torque.

A high-velocity zone forms around the convex surface of another blade of the three-and four-bladed turbines, which means that one more blade is providing positive torque. Thus, the torque of the multi-blade turbines declines more slowly, which contributes to a more stable torque output (see the curves plotted in Fig. 18). Another point to note is that observing the free surfaces in Fig. 19(b), multi-bladed turbines are more likely to cause wave breaking. This is the reason for the superharmonics apparent in the curves of the multi-bladed turbines in Fig. 18. Consequently, although the multi-bladed SHT-WECs operating under IPLS produce stable torque output, the two-bladed turbine is still the optimal choice because of the higher ECE and lower manufacturing cost. The remainder of this paper thus focuses on the two-bladed SHT-WEC.

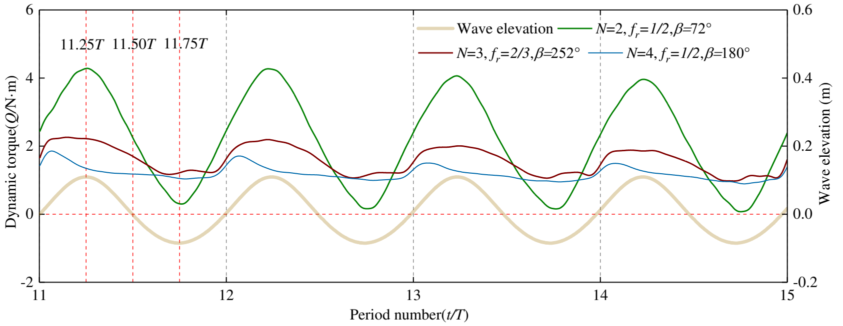

Fig. 18. Time history of the dynamic torque of SHT-WECs operating under IPLS with different blade numbers (*T*=1.3 s; *H*= 0.18m).

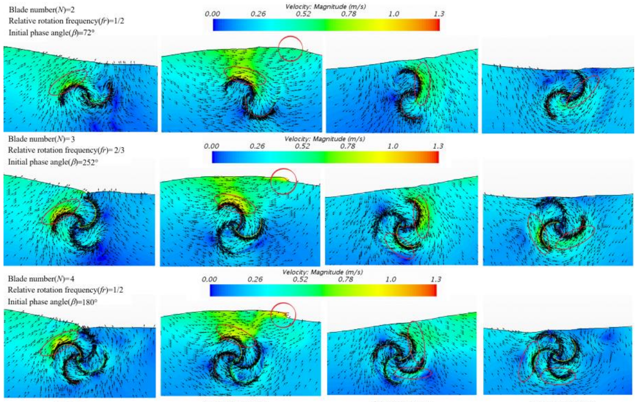

(a)11*T* (b)11*T*+0.25*T* (c)11*T*+0.5*T* (d)11*T*+0.75*T*

Fig. 19. Velocity vector and contours around the SHT-WECs with different blade numbers during one wave period (*T*=1.3 s; *H*= 0.18m).

5.3 Blade thickness

Figure 20 presents the performance curves for the two-bladed SHT-WEC (with parameters D=0.3 m, T=1.3s and H=0.18m), illustrating average torque (including the blade side and edge) and energy conversion efficiency as functions of blade thickness.

The torque trend on the blade edge shown in Fig. 20(a) exhibits a positive linear growth rate with regard to increasing blade thickness. However, the torque on the blade side presents an entirely opposite trend. When the blade thickness is increased above 3.5 mm, the torque working on the side even becomes negative. As a result, the total torque generated by the turbine slightly reduces with increasing blade thickness. The efficiency curve plotted in Fig.18(b) presents a similar trend, and the maximum ECE of 12.9% is obtained at $\delta = 0.0$ mm. The time history of dynamic torque in Fig. 21 shows the difference in contribution between the blade sides and edges for SHT-WECs with a 1.5 mm and 6 mm thickness. It is evident that the thinner turbine consistently maintains a higher overall torque output.

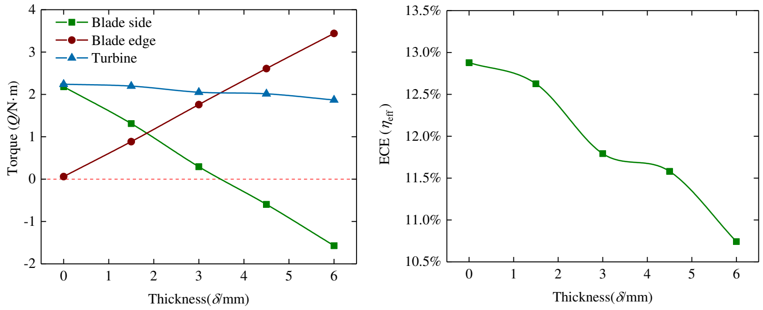

(a) Average torque(Q , N·m) (b) Energy conversion efficiency(η_{eff})

Fig. 20. Average torque and energy conversion efficiency of SHT-WECs operating under IPLS with different blade thicknesses. (T=1.3 s; H= 0.18m)

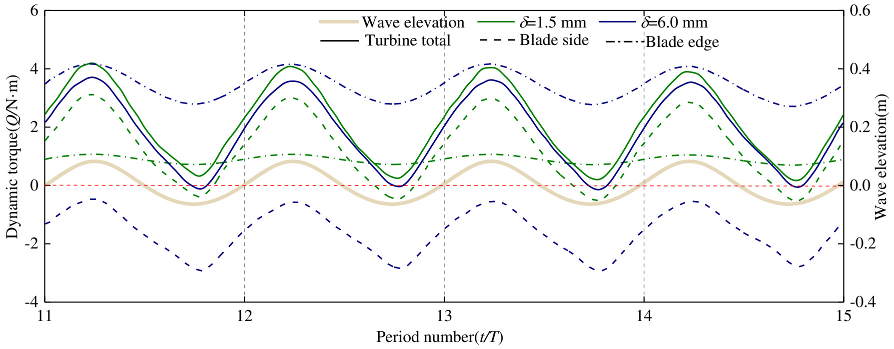

Fig. 21. Time history of the dynamic torque of SHT-WECs operating under IPLS with different blade thicknesses of 0.0015 m and 0.006 m (T=1.3 s; H= 0.18 m).

Although, as expected, the torque generated on the blade edges presents a noticeable growth with increasing thickness, the torque of the blade sides reduces even more, giving that the hypothesis of improving SHT-WEC performance by enlarging the blade thickness is not valid. In order to analyze the phenomenon mentioned above, the flow field around the SHT-WECs with different thicknesses are compared in Fig. 22(a) and Fig. 22(b). The flow around the two edges of different thicknesses is similar. The water particles collide with the blade edges perpendicular to their surfaces, so the torque increases proportionally to the blade thickness. The effect on the blade sides is harder to identify from the velocity fields (marked in Fig. 22). However, the differences can be clearly identified from the pressure distribution on the blade surfaces, as shown in Fig. 23. The blue blade of $\delta = 6.0$ mm is the advancing blade providing positive torque. The pressure on its concave surface is higher, and the pressure on the convex surface is lower than for the $\delta = 0.0$ mm blade, which means the blue blade of $\delta = 6.0$ mm provides more positive torque. But, because of the thickness, the projection of the concave surface of $\delta = 6.0$ mm in the x-direction is shorter. This is illustrated by marked red lines in Fig. 23(a) and Fig. 23(b). For the advancing blade, there is no pressure working on the concave surface in that region, only the negative pressure working on the convex surface. Analogously, for the returning blade, it can be observed that only the opposite force acts on the convex surface in the previously described region. The produced torque is thus significantly reduced. Consequently, the performance of SHT-WECs can not be improved by increasing the blade thickness as torque generation on the blade edges and sides are conflicting.

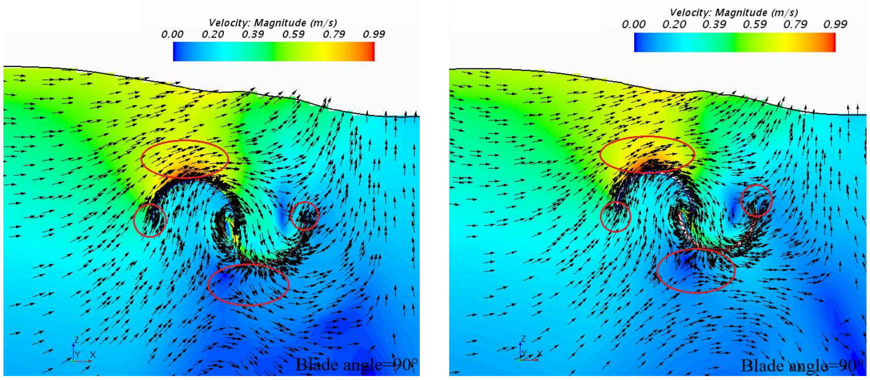

(a) $\delta = 0.0$ mm (b) $\delta = 6.0$ mm

Fig. 22 The velocity vector around the SHT-WEC of $\theta = 90^{\circ}$ with different thicknesses (T=1.3 s; H= 0.18m) .

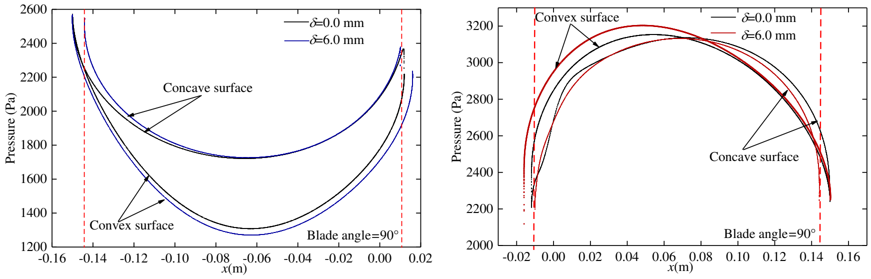

(a) Advancing blade (blue blade) (b) Returning blade (red blade)

Fig. 23 Pressure distribution on the blade sides with the thickness of 0.0 mm and 6 mm (T=1.3 s; H= 0.18m).

5.4 Turbine diameter (D)

Variations of the predicted average torque, power output, and ECE with different turbine diameters under the same wave conditions as in [28] (H=0.18 m and T=[1.3, 1.6, 1.9] s) are presented in Fig. 24. The average torque, power output, and ECE all increase with turbine diameter up to the maximum values obtained at a diameter of 0.45 m for the three different wave periods and then gradually decreases. As seen in Fig. 24(a), the average torque generated on the turbine under the wave period of 1.3 s is overall lower, and its maximum value was around 2.9 N·m. The other two curves (T=1.6

s and T=1.9 s) peaked around 3.8 N·m with similar values. However, due to the faster rotation speed associated with a shorter wave period, power generation for T=1.3 s surpasses T=1.9 s, as shown in Fig. 24(b). But because of the large torque gap between T=1.3 s and T=1.6 s, power generation for T=1.3 s is still lower than T=1.6s, and the highest value of T=1.6s is about 7.62W, as shown in Fig. 24(b). Then, as was also reported in [28], from Fig. 24(c) can be observed that the turbines generally perform more efficiently with decreasing wave periods, where the maximum values are 16.7% (T=1.3 s), 14.8% (T= 1.6 s), and 11.6% (T= 1.9 s). However, the difference is that the ECE drops sharply after the optimum diameter for shorter wave periods. As a result, after the diameter increases to around 0.5 m, the ECE of T=1.3 s shifts to be lower. The time history of the dynamic torques of three SHT-WECs with different diameters are plotted in Fig. 25. It is seen that the torques still vary periodically and in phase with the wave elevation. Moreover, the dynamic torque produced on the turbine of D=0.45 m always is higher compared to the other two diameters.

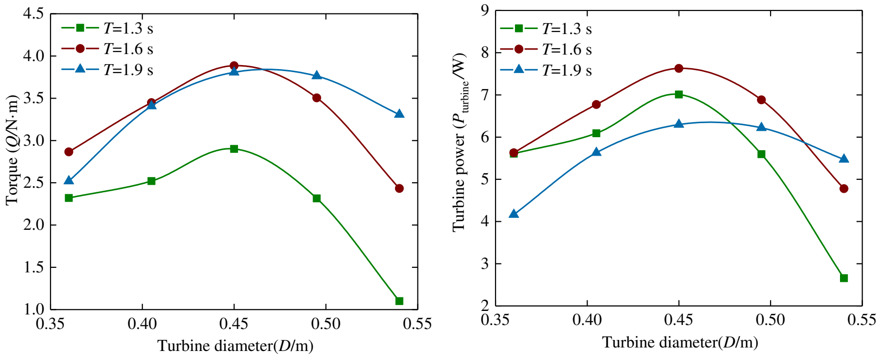

(a) Average torque(Q , N·m) (b) Power output(P_{turbine} ,W)

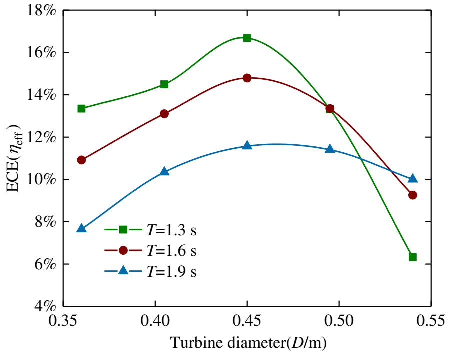

(c) Energy conversion efficiency(η_{eff})

Fig. 24. Average torque, power output, and energy conversion of SHT-WECs operating under IPLS with different turbine diameters (H=0.18m; T=1.3 s, 1.6 s, 1.9 s).

The simulations clearly illustrate that designing the turbine diameter to a proper value would significantly enhance the performance of SHT-WEC. Compared to the maximum ECE reported in [28] for the case of $D = 0.3$ m (12.4% for $T = 1.3$ s, 7.6% for $T = 1.6$ s, and 3.8% for $T = 1.9$ s), the ECEs are increased by 33%, 93%, and 200%, respectively. Fig. 26(a) shows the pressure distribution on the blade surfaces of the turbines projected on the x-axis with different diameters for the blade angle of 90° and the velocity contour. Although there is an overall pressure growth on the surfaces with the depth increase due to the fluid gravity, the torque working on the blade is determined by the pressure difference between the concave and the convex surfaces. When the blade size increases from 0.36m to 0.45m, the pressure differences of the blue blade (the advancing blade providing the positive torque) in the right region of the marked line are almost similar. But on the left, the pressure difference becomes larger, and even the longer part of the blade($D = 0.45\,\text{m}$) is still under positive pressure(a higher velocity zone can be identified around the concave surface as marked in the flow field), which means the torque is significantly increased. However, with the further increase in turbine diameter to 0.54 m, it can be seen in Fig. 26 that the overall pressure difference produced on the blue blade decreased. The pressure on the convex surface of the increased part(the left region, as marked) is shifted to larger(the velocity field around the convex surface turns slightly higher, as marked), generating significant negative torque. Moreover, observing the pressure distribution of the red blade (*D*=0.54 m), it is clear that a larger convex surface region is under higher pressure.

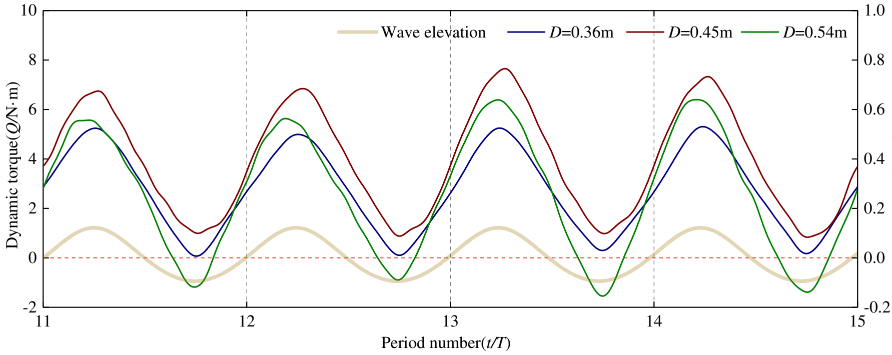

Fig. 25. Time history of the dynamic torque of SHT-WECs operating under IPLS with different turbine diameters of 0.36 m, 0.45 m, and 0.54 m (*H*=0.18 m and *T*=1.6 s).

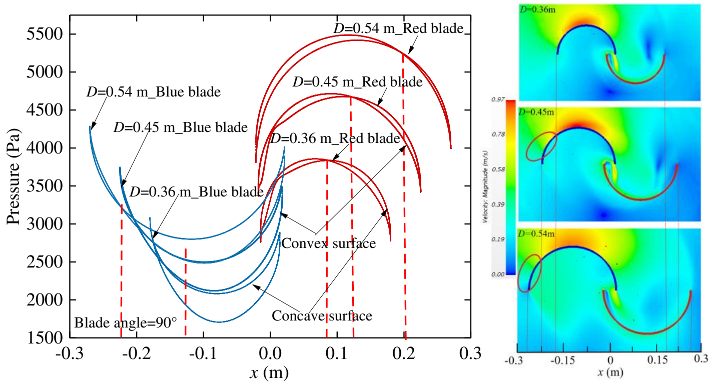

(a) Pressure distribution on the blade (b) Velocity contours around the turbines

Fig. 26. Pressure distribution on the blade surfaces and the velocity contour around the turbines with different diameters of 0.54 m, 0.45 m, and 0.36 m (*H*=0.18 m and *T*=1.6 s).

The following two facts account for the result. One is the high *TSR*. With the increase in blade size, the tip speed accelerates, and the position of the tip edge is farther away from the still water level, leading to the movement of the water particles around the tip edge decelerating. As a result, the blade rotates relatively quickly to the moving water particles around the blade tip to produce less or even negative torque. Another is the negative relative-short wavelength impact, which can not be neglected due to the wavelengths considered in this study all being less than 16.7*D*. During the initial phase of diameter increment from a smaller value, the positive effect stemming from the augmented tip speed ratio (*TSR*) is notably pronounced. However, with further growth in diameter, the wavelength becomes shorter relative to the turbine diameter, which means the negative RSWI worsens, seriously impacting the performance. This is the main reason causing the performance drop after optimum diameter, especially in a shorter wave period, leading to the ECE of T=1.3 s turning to be lower after the $D = 0.5$ m.

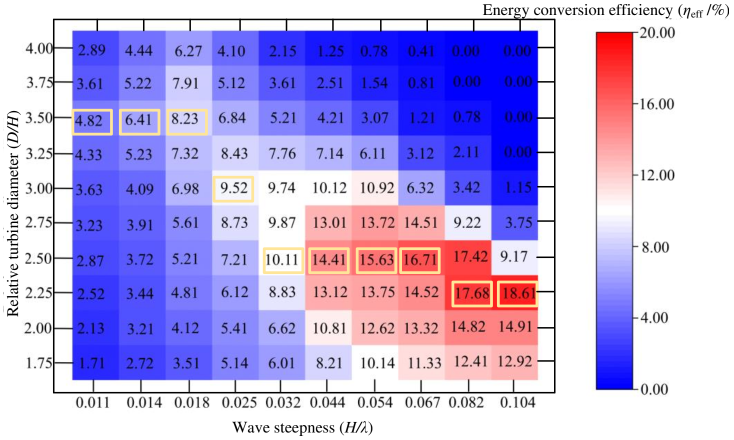

	0.011	0.014	0.018	0.025	0.032	0.044	0.054	0.067	0.082	0.104
4.00	2.89	4.44	6.27	4.10	2.15	1.25	0.78	0.41	0.00	0.00
3.75	3.61	5.22	7.91	5.12	3.61	2.51	1.54	0.81	0.00	0.00
3.50	4.82	6.41	8.23	6.84	5.21	4.21	3.07	1.21	0.78	0.00
3.25	4.33	5.23	7.32	8.43	7.76	7.14	6.11	3.12	2.11	0.00
3.00	3.63	4.09	6.98	9.52	9.74	10.12	10.92	6.32	3.42	1.15
2.75	3.23	3.91	5.61	8.73	9.87	13.01	13.72	14.51	9.22	3.75
2.50	2.87	3.72	5.21	7.21	10.11	14.41	15.63	16.71	17.42	9.17
2.25	2.52	3.44	4.81	6.12	8.83	13.12	13.75	14.52	17.68	18.61
2.00	2.13	3.21	4.12	5.41	6.62	10.81	12.62	13.32	14.82	14.91
1.75	1.71	2.72	3.51	5.14	6.01	8.21	10.14	11.33	12.41	12.92

Fig. 27. Heat map of the average energy conversion efficiency of SHT-WECs with different relative diameters under various wave steepness.

Although it was noticed that the turbines under the three wave periods all reached the maximum values at D=0.45 m, it can not conclude that the D=0.45m is the optimum diameter for all the wave conditions. Primarily, we know that the performance will be affected by the *TSR* and RSWI simultaneously. Thus, exploring the association of optimum diameter with wave height and wavelength is necessary. It aims to figure out the general guide for choosing the proper diameter according to the different wave conditions. The heat map of the average ECE(η_{eff}) of the turbine with different relative turbine diameters (D/H) grouped by wave steepness (H/λ) is plotted in Fig. 27. It shows the maximum ECEs of each wave steepness, as marked in Fig. 27, increase with H/λ, and are obtained at different D/H. Several principles can be identified from the variation trend of optimum D/H against wave steepness. There is a sort of overall growth in optimum D/H with the reduction of wave steepness, and the corresponding λ/D also increases. It is due to the restriction strength caused by the RSWI under lower wave steepness being less in enhancing the performance by increasing the D/H.

Furthermore, It is noteworthy here that there are three ranges of wave steepness where the obtained optimum D/H is constant ($0.082 \le H/\lambda \le 0.104$, $D/H = 2.25$; $0.032 \le H/\lambda \le 0.067$, $D/H = 2.5$; $0.011 \le H/\lambda \le 0.018$, $D/H = 3.5$). The stable ranges are due to the fact that although the restriction strength coming from RSWI is weakening with the wave steepness decrease, in the process of increasing the turbine diameter, the improvement from raising *TSR* is still not over the negative impact caused by RSWI. Thus the optimum H/λ is unchanged in the mentioned ranges of H/λ. Additionally, for the wave steepness range between 0.011 and 0.0118, the corresponding λ/D is close to or above 16.8, which means there is already no RSWI. The decrease in ECE with the further increase in turbine diameter is only due to the relatively high *TSR*(D/H). Thus, it can be deduced that the optimum D/H is constant at 3.5 when the wave steepness is less than 0.018. It is worthing to note when the SHT is proposed to operate in the wave steepness between the two stable ranges, the optimum D/H value is recommended to follow the higher range for the less RSWI. Consequently, designing the turbine diameter as the proper value according to wave conditions will effectively enhance the efficiency of SHT-WECs.

6. Conclusions

A systematic performance investigation employing two-phase RANS simulations was conducted to comprehensively analyze SHT-WECs operating under the optimal IPLS strategy within regular wave conditions. The study primarily aimed to assess the impact of crucial geometric parameters, including (i) the number of blades, (ii) blade thickness, and (iii) turbine diameter. The numerical wave tank was validated against a physical test in order to reliably estimate the energy harvesting performance of SHT-WECs in terms of the generated torque, power output, and energy conversion efficiency. The obtained simulation results of the time history of dynamic torques visualized flow fields and pressure distributions on blade surfaces are compared to illustrate the flow characteristics and the underlying mechanisms. The major conclusions to be drawn from the study are as follows:

- The efficiency generally increases proportionally with the wave height. However, the effect of wave period is not as straightforward as it is linked to the turbine diameter due to the so-called "relative-short wavelength impact" (RSWI) , caused by a non-uniform wave-induced velocity field acting over the turbine. The RSWI can, however, be neglected when the relative wavelength to turbine diameter (λ / D) is over approx. 17.
- Increasing blade thickness does not provide the expected improvement in efficiency. Although the torque generated by the blade edge increases with increasing blade thickness, the torque generated by the blade side becomes even more reduced. The blades are recommended to be manufactured as thin as possible.
- Although multi-bladed turbines operating under IPLS rotate faster, they exhibit worse performance due to a significantly reduced torque. For the four-bladed SHT-WEC rotating with $f_r = 3/4$, the maximum ECE decreases by 60% compared to the 2-bladed turbine.
- It was shown that the turbine diameter is a significant parameter affecting the performance of the SHT-WEC in terms of ECE. The maximum ECE of 18.6% is obtained at $D/H = 2.25$ for a wave steepness of 0.104. However, the influence mechanism is since the turbine determines the *TSR* and also is a key parameter for the RSWI. As a result, the optimal relative turbine diameter (D/H) is not constant but depends on the wave steepness.

Finally, the study presented a thorough investigation of geometric parameters and can be used as a guideline for designing SHT-WECs. However, please note that the results are applicable only for SHT-WECs operating under IPLS. IPLS has been proven to be the optimum operating strategy for regular waves [26], but more work is required to extend the results to irregular sea states.

Acknowledgment

This research was funded by the Science and Technology Innovation 2025 Major Project of Ningbo Science and Technology Bureau, grant number 2020Z076.

Reference:

[1] I. (2019), *World Energy Outlook 2019*. Paris: OECD Publishing 2019.

[2] R. (2020), "Renewable capacity statistics 2020," in "i," International Renewable Energy Agency (IRENA), Abu Dhabi2020.

[3] C. Zheng *et al.*, "An assessment of global ocean wave energy resources over the last 45 a," *Acta Oceanologica Sinica,* vol. 33, no. 1, pp. 92-101, 2014.

[4] D. Zhang, W. Li, and Y. Lin, "Wave energy in China: Current status and perspectives," *Renewable Energy,* vol. 34, no. 10, pp. 2089-2092, 2009.

[5] A. Clement *et al.*, "Wave energy in Europe: current status and perspectives," (in English), *Renewable & Sustainable Energy Reviews,* vol. 6, no. 5, pp. 405-431, Oct 2002.

[6] A. F. d. O. Falcão, "Wave energy utilization: A review of the technologies," *Renewable and Sustainable Energy Reviews,* vol. 14, no. 3, pp. 899-918, 2010.

[7] T. W. Heath, T J.T.; Boake, C B, " The design, construction and operation of the LIMPET wave energy

converter (Islay, Scotland)[Land Installed Marine Powered Energy Transformer]," presented at the 4. European wave energy conference, Aalborg, Denmark, 2001.

[8] O. I. Torre-Enciso Y, Lo´ pez de Aguileta LI, Marque´ s J, "Mutriku wave power plant: from the thinking out to the reality," presented at the Proceedings 8thEuropean Wave Tidal Energy Conference, 2009.

[9] M. F. Weber J, Parrish A, Robertson D, "Wavebob – research & development network and tools in the context of systems engineering," presented at the Proceed-ings of 8th European Wave Tidal Energy Conference, 2009.

[10] M. Kramer, Marquis, L., & Frigaard, P., "Performance Evaluation of the Wavestar Prototype," presented at the 9th ewtec 2011: Proceedings of the 9th European Wave and Tidal Conference, Southampton, UK, 2011.

[11] K. Budal and J. Falnes, "Wave power conversion by point absorbers: A Norwegian project," *International Journal of Ambient Energy,* vol. 3, no. 2, pp. 59-67, 2011.

[12] J. P. Kofoed, P. Frigaard, E. Friis-Madsen, and H. C. Sørensen, "Prototype testing of the wave energy converter wave dragon," (in English), *Renewable Energy,* vol. 31, no. 2, pp. 181-189, Feb 2006.

[13] S. S.J., "The S-rotor and its applications," *Mechanical Engineering,* 1931.

[14] P. K. Talukdar, A. Sardar, V. Kulkarni, and U. K. Saha, "Parametric analysis of model Savonius hydrokinetic turbines through experimental and computational investigations," *Energy Conversion and Management,* vol. 158, pp. 36-49, 2018.

[15] R. Ji, K. Sun, J. Zhang, R. Zhu, and S. Wang, "A novel actuator line-immersed boundary (AL-IB) hybrid approach for wake characteristics prediction of a horizontal-axis wind turbine," *Energy Conversion and Management,* vol. 253, p. 115193, 2022.

[16] S. A. Payambarpour, A. F. Najafi, and F. Magagnato, "Investigation of deflector geometry and turbine aspect ratio effect on 3D modified in-pipe hydro Savonius turbine: Parametric study," *Renewable Energy,* vol. 148, pp. 44-59, 2020.

[17] K. Golecha, T. I. Eldho, and S. V. Prabhu, "Influence of the deflector plate on the performance of modified Savonius water turbine," *Applied Energy,* vol. 88, no. 9, pp. 3207-3217, 2011.

[18] E. Fatahian, F. Ismail, M. H. H. Ishak, and W. S. Chang, "The role of wake splitter deflector on performance enhancement of Savonius wind turbine," *Physics of Fluids,* vol. 34, no. 9, p. 095111, 2022.

[19] R. V. Bethi, S. Mitra, and P. Kumar, "An OpenFOAM based study of Savonius turbine arrays in tunnels for power maximisation," *Renewable Energy,* vol. 179, pp. 1345-1359, 2021.

[20] K. Sun, R. Ji, J. Zhang, Y. Li, and B. Wang, "Investigations on the hydrodynamic interference of the multi-rotor vertical axis tidal current turbine," *Renewable Energy,* vol. 169, pp. 752-764, 2021.

[21] S. N. Bora, S. Das, M. H. Meylan, S. Saha, and S. Zheng, "Time-dependent water wave scattering by a marine structure consisting of an array of compound porous cylinders," *Physics of Fluids,* vol. 35, no. 7, 2023.

[22] M. M. Kamal and R. P. Saini, "A numerical investigation on the influence of savonius blade helicity on the performance characteristics of hybrid cross-flow hydrokinetic turbine," *Renewable Energy,* vol. 190, pp. 788-804, 2022.

[23] A. Kumar and R. P. Saini, "Performance parameters of Savonius type hydrokinetic turbine – A Review," *Renewable and Sustainable Energy Reviews,* vol. 64, pp. 289-310, 2016.

[24] C. M. Chan, H. L. Bai, and D. Q. He, "Blade shape optimization of the Savonius wind turbine using a genetic algorithm," *Applied Energy,* vol. 213, pp. 148-157, 2018.

[25] H. Fatahian, Z. Mohamed-Kassim, and W. S. Chang, "Insights into the flow dynamics and rotor performance of a Savonius turbine with dynamic venting using controllable flaps," *Physics of Fluids,* vol.

34, no. 12, p. 127109, 2022.

[26] J. Yao, F. Li, J. Chen, Z. Yuan, and W. Mai, "Parameter Analysis of Savonius Hydraulic Turbine Considering the Effect of Reducing Flow Velocity," *Energies,* vol. 13, no. 1, p. 24, 2019.

[27] S. Roy, R. Das, and U. K. Saha, "An inverse method for optimization of geometric parameters of a Savonius-style wind turbine," *Energy Conversion and Management,* vol. 155, pp. 116-127, 2018.

[28] F. Li, J. Yao, J. Chen, H. Jin, and Z. Yuan, "Performance analysis of Savonius hydrokinetic turbine capturing wave energy under different operating strategies," *Energy Conversion and Management,* vol. 251, p. 115006, 2022.

[29] D. D. Prasad, M. R. Ahmed, and Y.-H. Lee, "Studies on the performance of Savonius rotors in a numerical wave tank," *Ocean Engineering,* vol. 158, pp. 29-37, 2018.

[30] M. R. Ahmed, M. Faizal, and Y.-H. Lee, "Optimization of blade curvature and inter-rotor spacing of Savonius rotors for maximum wave energy extraction," *Ocean Engineering,* vol. 65, pp. 32-38, 2013.

[31] M. Tutar and I. Veci, "Experimental study on performance assessment of Savonius rotor type wave energy converter in an experimental wave flume," *IET Renewable Power Generation,* vol. 10, no. 4, pp. 541-550, 2016.

[32] M. A. Zullah and Y.-H. Lee, "Performance evaluation of a direct drive wave energy converter using CFD," *Renewable Energy,* vol. 49, pp. 237-241, 2013.

[33] M. Mosbahi, A. Ayadi, Y. Chouaibi, Z. Driss, and T. Tucciarelli, "Performance study of a Helical Savonius hydrokinetic turbine with a new deflector system design," *Energy Conversion and Management,* vol. 194, pp. 55-74, 2019.

[34] V. Patel, G. Bhat, T. I. Eldho, and S. V. Prabhu, "Influence of overlap ratio and aspect ratio on the performance of Savonius hydrokinetic turbine," *International Journal of Energy Research,* vol. 41, no. 6, pp. 829-844, 2017.

[35] Y. Liu and Q. Xiao, "Development of a fully coupled aero-hydro-mooring-elastic tool for floating offshore wind turbines," *Journal of Hydrodynamics,* vol. 31, no. 1, pp. 21-33, 2019.

[36] L. B. E. Jones W P "The Prediction of Laminarization with a Two-Equation Model of Turbulence," *International Journal of Heat & Mass Transfer,* vol. 15, no. 2, pp. 301-314, 1972.

[37] D. D. Prasad, M. R. Ahmed, Y.-H. Lee, and R. N. Sharma, "Validation of a piston type wave-maker using Numerical Wave Tank," *Ocean Engineering,* vol. 131, pp. 57-67, 2017.

[38] J. D. Fenton, "A Fifth-Order Stokes Theory for Steady Waves," *Journal of Waterway Port Coastal and Ocean Engineering,* vol. 111, no. 2, pp. 216-234, 1985.

[39] J. Choi and S. B. Yoon, "Numerical simulations using momentum source wave-maker applied to RANS equation model," *Coastal Engineering,* vol. 56, no. 10, pp. 1043-1060, 2009.

[40] M. Tutar and I. Veci, "Performance analysis of a horizontal axis 3-bladed Savonius type wave turbine in an experimental wave flume (EWF)," *Renewable Energy,* vol. 86, pp. 8-25, 2016.